Thermo-Mechanical Responses of Zircaloy-4 Cladding in a Fuel Rod Loaded with Axially-Shielded Burnable Absorber

Yongse Kim [a], Yunseok Jeong [a], and Yonghee Kim [a*]
[a]*Nuclear and Quantum Engineering, KAIST*
[*]*Corresponding author: yongheekim@kaist.ac.kr*

Keywords : Axially-shielded burnable absorber, Zircaloy-4 cladding, thermo-mechanical analysis, fuel-cladding mechanical interaction, irradiation-induced fuel swelling

1. Introduction

The axially-shielded burnable absorber (ABA) has been proposed for soluble boron-free small modular reactors (SMRs) [1]. It employs localized UO_2-Gd_2O_3 integral gadolinia (IGD) pellets at selected axial positions to control gadolinium depletion through axial self-shielding. Previous studies demonstrated the neutronic feasibility of the ABA concept in the initial and equilibrium cycles [1–3] and evaluated its thermal-hydraulic characteristics [1,3].

The axially non-uniform fuel composition and power distribution of the ABA produce local variations in fuel and cladding temperatures. However, the corresponding thermo-mechanical response of the Zircaloy-4 cladding has not been explicitly evaluated. In this study, the thermo-mechanical response of Zircaloy-4 cladding in the ABA rod and a reference rod without a burnable absorber (NoBA) was evaluated using ANSYS Fluent and Mechanical analyses to identify ABA-specific cladding stress characteristics and potential structural concerns. The BOC analysis focused on the cladding response to the ABA-induced thermal field, whereas the EOC analysis additionally considered irradiation-induced fuel swelling and fuel-cladding mechanical interaction.

2. Methods

2.1 Thermal-Hydraulic Analysis

The baseline fuel-rod dimensions were adopted from the previous ABA study [3], and the major geometry and coolant conditions used in the present analysis are summarized in Table I. A steady-state 2D axisymmetric conjugate heat-transfer analysis was performed using ANSYS Fluent with single-phase pressurized water and the standard $k-\varepsilon$ model with enhanced wall treatment. Temperature-dependent material properties were specified for all modeled materials. The helium gap was modeled by conduction, with radiation neglected because its contribution was below 1%. Contact-pressure effects, gap-width variations, and fission-gas composition changes were not included in the gap heat-transfer model.

The BOC and EOC cases represent fresh and twice-burned fuel rods, respectively, in the two-batch equilibrium core. Axial heat-generation distributions for both rods were obtained from Serpent 2 calculations [4], with the ABA distribution applied according to the ABA axial loading configuration. The ABA average volumetric heat-generation rates were 3.2703×10^8 W/m³ at BOC and 2.8471×10^8 W/m³ at EOC, with the total NoBA rod power matched to the corresponding ABA case at each cycle condition.

At BOC, the fuel thermal conductivity was evaluated as a function of temperature and gadolinia content using fresh-fuel properties corresponding to zero burnup. At EOC, local burnup distributions obtained from Serpent 2 depletion calculations were additionally considered in the fuel thermal conductivity [5], with the ABA and NoBA rods having the same rod-average burnup of 48.81 GWd/tU. The resulting temperature fields were mapped to the ANSYS Mechanical structural model using nodal temperature data.

Table I: Fuel-rod geometry and operating conditions

Parameter	Value
Active fuel length	2.4 m
Fuel radius	4.0958 mm
Initial radial fuel-cladding gap	82.5 μm
Cladding thickness	0.5715 mm
Coolant annulus width	2.3581 mm
Coolant pressure	15 MPa
Coolant inlet temperature	569.41 K
Coolant inlet velocity	3.3568 m/s

2.2 Structural Analysis

A 2D axisymmetric structural analysis was performed using the Static Structural module of ANSYS Mechanical. For all BOC and EOC cases, the fuel and cladding were explicitly included in the structural model. The 2.4-m active fuel column was modeled as an axially continuous fuel region, with the UO_2 and IGD fuel regions assigned according to the ABA axial loading configuration shown in Fig. 1. The fuel-cladding interface was modeled as frictionless contact for both the

ABA and NoBA rods. A 0.25 mm axial element size with 14 fuel and 10 cladding radial divisions was used for all cases based on mesh-refinement calculations.

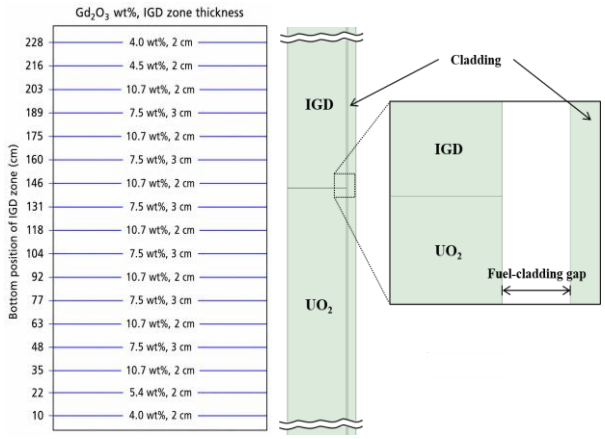


Fig. 1. ABA axial configuration and 2D axisymmetric structural model.

Zircaloy-4 thermal expansion and elastic moduli were evaluated using [5], with the elastic moduli dependent on temperature and fast-neutron fluence. BOC fluence was set to zero, whereas both EOC rods used a representative PWR axial distribution of 6.58×10^{25}–9.75×10^{25} n/m² corresponding to an assembly-average burnup of 50 GWd/tU [6]. Across this EOC fluence range, the fluence correction factor applied to both elastic moduli varied by only approximately 0.02%. A stress-free temperature of 293.15 K was assigned to the cladding.

Fuel thermal expansion was evaluated using [5] with a stress-free temperature of 300 K. The Young's modulus of UO_2 was evaluated as a function of temperature and burnup [6], whereas that of UO_2–Gd_2O_3 was evaluated using the temperature-, gadolinia-content-, and porosity-dependent model presented by Evans et al. [7]. At EOC, the burnup-dependent factor proposed by Cappia et al. [8] to account for the apparent softening of irradiated UO_2 was additionally applied to the UO_2–Gd_2O_3 regions as an approximation.

At BOC, no irradiation-induced fuel swelling was applied. At EOC, solid swelling was evaluated as a function of local burnup, and gaseous swelling as a function of local burnup and temperature [5]. For the 10.7 wt% IGD regions, the MatLib UO_2-Gd_2O_3 fuel-property correlations used in this study were slightly extrapolated beyond their documented 10 wt% gadolinia applicability limit. To assess the influence of irradiation swelling, the NoBA total irradiation-swelling field was mapped onto the ABA fuel in an additional EOC sensitivity case.

The coolant pressure in Table I was applied to the cladding outer surface, while the initial helium fill pressure of 2.0 MPa at 293.15 K yielded internal pressures of approximately 4.92 MPa at BOC and 4.80 MPa at EOC assuming ideal-gas behavior and negligible volume change. Axial displacement at the lower end was constrained, while expansion toward the upper end was allowed. All axial distributions are plotted against the current (deformed) axial coordinate y.

Because the accumulated irradiation creep-down of the Zircaloy-4 cladding was not explicitly simulated, a common radial contact offset was applied to both rods at EOC. Lee et al. reported a 70–75 μm diametral decrease for 10.72-mm Zircaloy-4 rods [9], corresponding to approximately 0.65–0.70% diametral creep strain. Scaling this range to the present 9.50-mm cladding gives a radial reduction of approximately 31–33 μm; therefore, 33 μm was used. The remaining fuel-cladding gap was evaluated from the relative radial displacements of the fuel outer surface and cladding inner surface as

$$g_{rem(y)} = \max\left[0, \left(g_0 - \delta_{off}\right) + u_{(r,clad,in)(y)} - u_{(r,fuel,out)(y)}\right] \quad (1)$$

where $g_0 = 82.5\ \mu$m is the initial radial gap and $\delta_{\mathrm{off}} = 33.0\ \mu$m is the EOC contact offset.

Cladding inner-surface stresses were examined to characterize the local mechanical response associated with fuel-cladding gap/contact transitions. For EOC yielding assessment, the maximum through-wall equivalent stress was compared with the minimum through-wall Zircaloy-4 yield stress evaluated using the Geelhood–Beyer correlation [6] with CW = 0.50, ΔO = 0.0012 kg O/kg Zry, and a strain rate of 10^{-4} s^{-1}.

3. Results and Discussion

3.1 BOC Thermo-Mechanical Response

Fig. 2 shows the BOC cladding inner-surface temperature and stress distributions for the ABA and NoBA rods. The NoBA temperature varies smoothly, whereas the ABA rod exhibits pronounced local temperature variations associated with its heterogeneous power distribution. No fuel-cladding contact occurred at BOC. The axial and hoop stresses show a similar ABA–NoBA contrast, with repeated local variations in the ABA rod; the hoop stress remains compressive under the net external pressure loading. In contrast, the radial stress remains near −5.5 MPa in both rods and is predominantly governed by pressure loading.

The maximum absolute local differences between the ABA and NoBA rods were approximately 6.95 MPa for the axial stress and 7.19 MPa for the hoop stress, both occurring near an axial position of 1.06 m. The maximum ABA–NoBA temperature difference also occurred near the same axial position. Moreover, the axial distribution of the ABA–NoBA temperature difference, ΔT, was strongly inversely correlated with those of the axial- and hoop-stress differences, $\Delta\sigma_{\mathrm{axial}}$ and $\Delta\sigma_{\mathrm{hoop}}$, with Pearson correlation coefficients of −0.989 for both stress components. Together with the absence of fuel-cladding contact at BOC, these results indicate that the localized ABA–NoBA cladding stress differences are primarily associated with the ABA-induced non-uniform thermal field. Nevertheless, the magnitude of these thermally

induced stress differences remained small under BOC conditions.

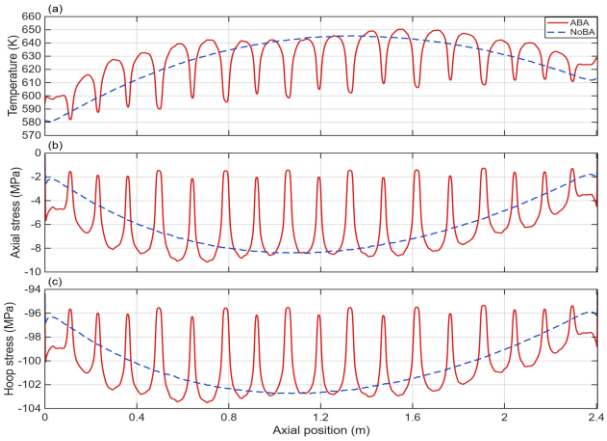


Fig. 2. BOC cladding inner-surface distributions of (a) temperature, (b) axial stress, and (c) hoop stress for the ABA and NoBA rods.

3.2 EOC Thermo-Mechanical Response

Fig. 3 presents the axial distributions of local fuel burnup, cladding inner-surface temperature, and the remaining fuel-cladding gap defined by Eq. (1). Despite the same rod-average EOC burnup, the ABA rod exhibits a strongly non-uniform burnup distribution, with much lower burnups in the IGD regions and clearly higher local burnups in the UO_2 regions, resulting in a maximum burnup of 56.80 GWd/tU compared with 52.84 GWd/tU for NoBA. This heterogeneous burnup distribution contributes to greater swelling in the higher-burnup UO_2 regions while promoting localized gap reopening in several lower-burnup IGD regions, thereby producing repeated local gap/contact transitions. The fuel-cladding gap was closed over approximately 84.0% of the ABA rod, compared with 91.8% for the NoBA rod.

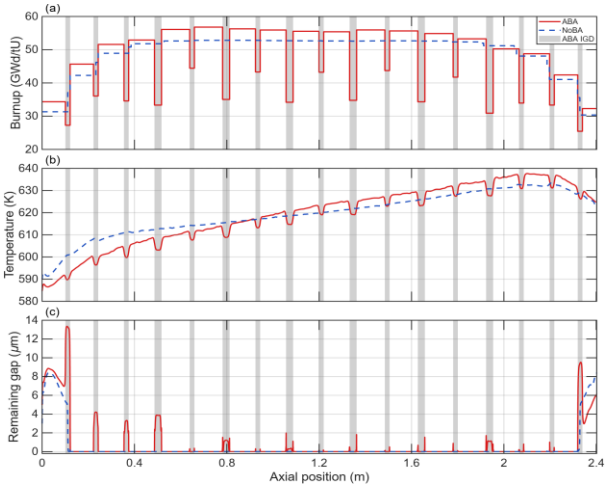


Fig. 3. EOC axial distributions of (a) fuel burnup, (b) cladding inner-surface temperature, and (c) remaining fuel-cladding gap. Gray shading indicates ABA IGD regions.

In the structural analysis, irradiation-induced fuel swelling and thermal expansion were evaluated using the calculated burnup and temperature fields, resulting in extensive fuel-cladding mechanical interaction. As shown in Fig. 4 and Table II, the ABA rod exhibited substantially larger and more spatially heterogeneous inner-surface stresses than those in the NoBA rod, with the largest axial and radial differences occurring near IGD boundaries and the largest hoop-stress difference within a 7.5 wt% IGD region. In the mid-to-upper axial region (1.2–2.1 m), high local burnup in the ABA UO_2 regions promoted solid and gaseous swelling, while high fuel temperatures further enhanced gaseous swelling and thermal expansion. These contributions increased radial fuel displacement and contact loading, producing more compressive radial stresses and higher tensile hoop stresses than in NoBA, with the ABA hoop stress reaching its maximum at 1.769 m.

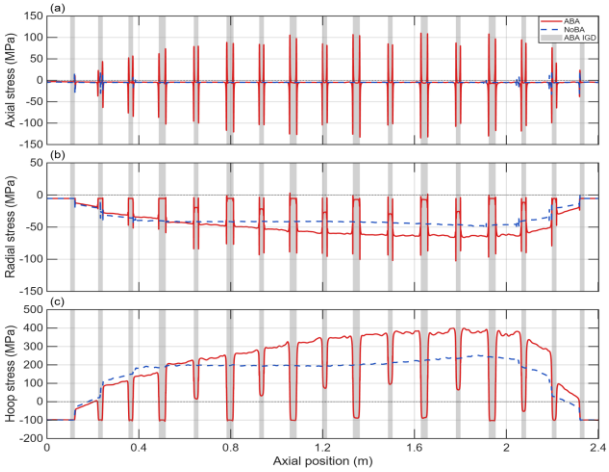


Fig. 4. EOC cladding inner-surface stress distributions for the ABA and NoBA rods: (a) axial, (b) radial, and (c) hoop stress. Gray shading indicates ABA IGD regions.

Table II: Maximum EOC ABA–NoBA cladding stress differences

Stress	Max. $\|\Delta\sigma\|$ (MPa)	Axial position (m)
Axial	130.0	1.627
Radial	61.6	2.198
Hoop	348.6	1.928

Fig. 5 examines a selected 7.5 wt% IGD region centered near 1.938 m, which showed the largest combined normalized RMS ABA–NoBA stress difference among the interior IGD regions. The ABA rod exhibits substantially larger local stress excursions than the NoBA rod near the IGD boundaries, where the local fuel-cladding state transitions between contact and gap. The abrupt change in radial cladding deformation between the contacted UO_2 region and the open-gap IGD region induces local shell bending, which produces the sharp compressive-to-tensile reversal in the inner-

surface axial stress. The radial stress primarily reflects the corresponding change in normal contact loading, while the hoop stress changes from large tensile values in the contacted UO_2 region to a compressive state as the fuel-induced circumferential loading is removed. Within the open-gap portion of the IGD region, the ABA radial and hoop stresses return to approximately −5.5 MPa and −100 MPa, respectively, comparable to their no-contact levels at BOC.

In the "ABA (NoBA swelling)" sensitivity case shown in Fig. 5, the NoBA total irradiation-swelling field was mapped onto the ABA fuel while retaining the ABA temperature and burnup fields and UO_2/IGD fuel configuration. Within the local region shown in Fig. 5, this substitution reduced the RMS ABA–NoBA stress differences by 94.8%, 92.3%, and 92.1% for the axial, radial, and hoop stresses, respectively. These substantial reductions indicate that the ABA–NoBA difference in total irradiation swelling is the dominant contributor to the local EOC stress differences, while the remaining differences reflect the combined effects of the ABA-specific thermal response and material heterogeneity.

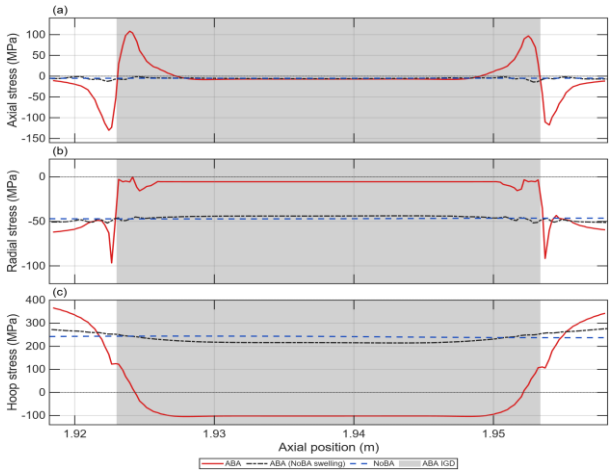


Fig. 5. Local EOC cladding inner-surface stress distributions around the selected ABA IGD region centered at 1.938 m for ABA, ABA (NoBA swelling), and NoBA: (a) axial, (b) radial, and (c) hoop stress. Gray shading indicates the ABA IGD region.

Although the ABA rod showed larger local stress excursions, the maximum through-wall equivalent stresses were 438.6 MPa for ABA and 284.0 MPa for NoBA. The corresponding minimum through-wall yield-stress profiles remained above the equivalent-stress profiles at all axial positions, with minima of 575.4 MPa for ABA and 576.7 MPa for NoBA. Therefore, despite the larger local cladding stresses in the ABA rod, no cladding yielding was indicated under the present EOC conditions.

4. Conclusions

At BOC, no fuel-cladding contact occurred, and the ABA-induced non-uniform thermal field produced localized axial- and hoop-stress variations compared with the smooth NoBA response, while the radial stress was only weakly affected. These differences were primarily associated with the ABA-specific thermal heterogeneity and remained limited in magnitude.

At EOC, fuel swelling and thermal expansion produced extensive fuel-cladding mechanical interaction, and the heterogeneous local burnup distribution in the ABA rod led to a non-uniform irradiation-swelling field, resulting in more spatially varying gap/contact states and larger local stress excursions than in NoBA. The sensitivity analysis in the examined IGD region showed that the ABA–NoBA difference in total irradiation swelling was the dominant contributor to the local EOC stress differences. Thus, the ABA configuration increases the local magnitude and spatial heterogeneity of the cladding stresses, but no cladding yielding was indicated under the conditions considered.

Further work should incorporate thermo-mechanical feedback on gap heat transfer and investigate the effects of ABA-induced thermal heterogeneity on cladding corrosion and hydrogen uptake.

REFERENCES

[1] Y. Jeong, J. Ryu, D. Choi, Y. Lee, and Y. Kim, "Axially-shielded Burnable Absorber (ABA) for Soluble Boron-Free SMR: Neutronics Feasibility in the Initial Cycle," Transactions of the Korean Nuclear Society Autumn Meeting, 2025.
[2] Y. Jeong, J. Ryu, and Y. Kim, "Neutronics Performance of Axially-shielded Burnable Absorber (ABA) in the Equilibrium Cycle of Soluble Boron-Free SMR," Transactions of the Korean Nuclear Society Spring Meeting, 2026.
[3] Y. Jeong, A Novel Axially-shielded Burnable Absorber (ABA) Development for Soluble Boron-Free Small Modular Reactor, Ph.D. Dissertation, KAIST, 2026.
[4] J. Leppänen, M. Pusa, T. Viitanen, V. Valtavirta, and T. Kaltiaisenaho, "The Serpent Monte Carlo code: Status, development and applications in 2013," Annals of Nuclear Energy, Vol. 82, pp. 142–150, 2015.
[5] K. J. Geelhood, W. G. Luscher, L. Kyriazidis, C. E. Goodson, J. Corson, J. J. Whitman, and D. F. Wray, MatLib-1.2.1: Nuclear Material Properties Library, PNNL-35702, Pacific Northwest National Laboratory, 2024.
[6] K. J. Geelhood and C. E. Beyer, Used Nuclear Fuel Loading and Structural Performance Under Normal Conditions of Transport – Supporting Material Properties and Modeling Inputs, FCRD-UFD-2013-000123, U.S. Department of Energy, 2013.
[7] J. A. Evans, M. D. DeHart, K. D. Weaver, and D. D. Keiser, "Burnable absorbers in nuclear reactors – A review," Nuclear Engineering and Design, Vol. 391, 111726, 2022.
[8] F. Cappia, D. Pizzocri, M. Marchetti, A. Schubert, P. Van Uffelen, L. Luzzi, D. Papaioannou, R. Macián-Juan, and V. V. Rondinella, "Microhardness and Young's modulus of high burn-up UO_2 fuel," Journal of Nuclear Materials, Vol. 479, pp. 447–454, 2016.
[9] B.-H. Lee, Y.-H. Koo, J.-S. Cheon, and D.-S. Sohn, "Modeling of creep behavior of Zircaloy-4 by considering metallurgical effect," Annals of Nuclear Energy, Vol. 29, No. 1, pp. 1–12, 2002.